Effect of UV-Ozone-Activated NiO_x on Co-SAM Coverage and Precursor-Solvent Stability in Inverted Perovskite Solar Cells

PREPARED BY

Bader Alshammari

Bader.Alshammari@Kaust.edu.sa

MENTOR

Kholood Bokhari

Kholood.Bokhari@Kaust.edu.sa

SUPERVISOR

Prof. Osman Bakr

Osman.Bakr@Kaust.edu.sa

KAUST Academy | 2026

Abstract

The MeO-2PACz+TBA co-self-assembled monolayer was developed on bare ITO, where a carboxylic-acid co-adsorbent disperses phosphonic-acid clusters and improves layer uniformity. Whether that benefit survives transfer to a NiO_x buried interface, and whether it depends on activating the oxide first, has not been established. Here water contact angle is used as a direct probe of the interface across a 2×2 matrix of additive and UV-ozone activation, measured both on the as-deposited monolayer and after exposure to the bare DMF:DMSO precursor solvent, with p–i–n devices fabricated on three of the four conditions. The additive improved coverage on NiO_x in all four comparisons, raising the contact angle by 13.6 to 26.2°. Activation, not the additive, controlled solvent stability: it reduced the solvent-induced angle loss from 16.6–20.7° to 3.0–4.8°, while the additive changed it by at most 4.1°. The interaction ran opposite to the acid–hydroxyl anchoring mechanism proposed at the outset — activation narrowed rather than widened the additive's advantage — which is the behaviour expected of a dispersant correcting incomplete coverage. Devices support this less strongly than the substrate data: the best co-SAM cell reached 18.60% against 17.75% for the best control, but open-circuit voltage separated the two groups without overlap (1.125–1.148 V versus 1.068 V across six devices and two runs) at unchanged photocurrent, and the control was far less reproducible, ranging from no functional pixel to 17.75% across three substrates. X-ray diffraction and electron microscopy find the same perovskite phase, residual PbI_2, optical gap and 115–118 nm grain size on both interfaces, so the performance difference was not produced by changing the absorber; photoluminescence from the co-SAM films is 1.35× brighter with no overlap between the groups, consistent with reduced non-radiative recombination at the contact. Coverage and solvent stability are separate properties of the buried interface, the co-adsorbent and the surface activation act principally on different ones, and a working monolayer on NiO_x requires both.

Contents

Abstract **i**

Acknowledgments **iii**

1 Introduction **1**

2 Methodology **6**
2.1 Overview . . . 6
2.2 Substrate preparation and NiO_x deposition . . . 7
2.3 UV-ozone activation . . . 7
2.4 Monolayer deposition . . . 7
2.5 Contact-angle measurement . . . 7
2.6 Device fabrication . . . 7
2.7 Characterisation overview . . . 8
2.8 Film characterisation . . . 8
2.9 Device characterisation . . . 9

3 Results **10**
3.1 Step 0: UV-ozone activation of bare NiO_x . . . 10
3.2 TBA raises the contact angle under every condition . . . 10
3.3 UV-ozone activation dominates solvent stability . . . 10
3.4 The additive's advantage is smaller on activated NiO_x . . . 11
3.5 Device performance . . . 12
3.6 The absorber itself is unchanged; only the interface differs . . . 13

4 Discussion **17**
4.1 Coverage and solvent stability are independent axes . . . 17
4.2 The interaction runs against the initial hypothesis . . . 17
4.3 What the devices do and do not show . . . 17
4.4 The film data localise the effect to the interface . . . 18
4.5 What cannot yet be concluded . . . 18

5 Limitations and Future Work **19**
5.1 Limitations . . . 19
5.2 Future work . . . 20

6 Conclusion **21**

References **22**

Acknowledgments

We gratefully acknowledge KAUST and KAUST Academy for their support and facilities, and Dr. Sultan Albarakaty for his guidance.

1 Introduction

Perovskite solar cells (PSCs) have reached certified power conversion efficiencies (PCE) above 26%, and the inverted (p-i-n) architecture is now the leading platform for reaching that level while remaining compatible with low-temperature, scalable processing and tandem integration [1, 2]. In this architecture the hole-transport layer (HTL) sits directly beneath the perovskite absorber, so it sets both the energy-level alignment at the buried interface and the surface the perovskite nucleates on. Its quality has a first-order effect on efficiency and operational stability.

Self-assembled monolayers (SAMs) of carbazole-phosphonic acids, most commonly MeO-2PACz, are increasingly used as alternatives to bulkier polymeric HTLs because they form an ultrathin, energetically well-matched contact with minimal parasitic absorption [3, 4]. Their characteristic failure mode is coverage: MeO-2PACz aggregates into clusters and micelles during deposition, leaving pinholes where the substrate is left bare. Those pinholes allow direct substrate–perovskite contact and act as shunting and non-radiative recombination sites, which caps the fill factor and the batch-to-batch reproducibility the device can reach.

Liu et al. addressed this by co-depositing MeO-2PACz with a small benzoic-acid additive, 4-(trifluoromethyl)benzoic acid (TBA) [5]. The additive interacts with MeO-2PACz, breaking up clusters so the layer deposits more uniformly, and it improves energy-level alignment with the perovskite. The reported result is substantial: PCE rising from 21.34% to 23.31%, with roughly 90% of the initial efficiency retained under continuous 1-sun operation. Critically for this project, that work was performed on bare ITO, activated by a ten-minute plasma treatment.

Our laboratory does not use bare ITO. Its baseline hole-transport stack places the SAM on top of a NiO_x underlayer – an architecture that is itself mature and well published, with certified efficiencies above 25% reported for NiO_x+SAM bilayers [6]. MeO-2PACz specifically has already been deposited on sputtered NiO_x, where it enlarged perovskite domains and passivated NiO_x surface defects [7]; that work is the direct precedent for our control condition. We therefore make no novelty claim for the NiO_x+SAM architecture, nor for MeO-2PACz on NiO_x. What has not been reported, to our knowledge, is the MeO-2PACz+TBA *co-SAM* deposited on a NiO_x surface.

The co-adsorbent strategy itself is a recognised class rather than a one-off. Li et al. [8] report a second trifluoromethyl-bearing carboxylic acid, PyCA-3F, co-adsorbed with 2PACz, where the carboxylate anchors to the substrate while the CF_3 group extends outward, suppressing SAM aggregation and raising work function. That study was performed on ITO, and it makes the mechanistic premise behind TBA considerably less speculative — while also making clear that the novelty here rests on the specific molecule–substrate pairing, not on the idea of an acid co-adsorbent.

That substitution is not cosmetic. TBA carries a carboxylic acid group, and carboxylic acids bind metal-oxide surfaces through surface hydroxyl (–OH) sites [7, 9], so the additive's behaviour may depend on the surface chemistry it encounters.

UV-ozone treatment of NiO_x is reported to lower the water contact angle from 45.6° to approximately 25° and to alter conductivity, non-stoichiometry and valence-band energy, with an optimum near five minutes of exposure [10]. Surface hydroxyl generation on NiO_x has been demonstrated for hydrogen-peroxide treatment, where the resulting hydroxyl groups promote SAM bonding [6, 11]. A corresponding increase in hydroxyl density under UV-ozone is plausible but has not been measured here, and is therefore treated as a working assumption rather than an established result.

The experiment is well posed under either interpretation: an acid-bearing additive and a purely dispersive one need not respond equally to surface activation, and the ±UVO comparison measures that difference directly. Attributing any observed difference specifically to hydroxyl density would require O 1s X-ray photoelectron spectroscopy before and after treatment, which lies outside the present scope.

A second issue applies to any SAM, and to co-SAMs in particular. Strongly polar precursor solvents are known to desorb SAMs that are held to the substrate by hydrogen bonding rather

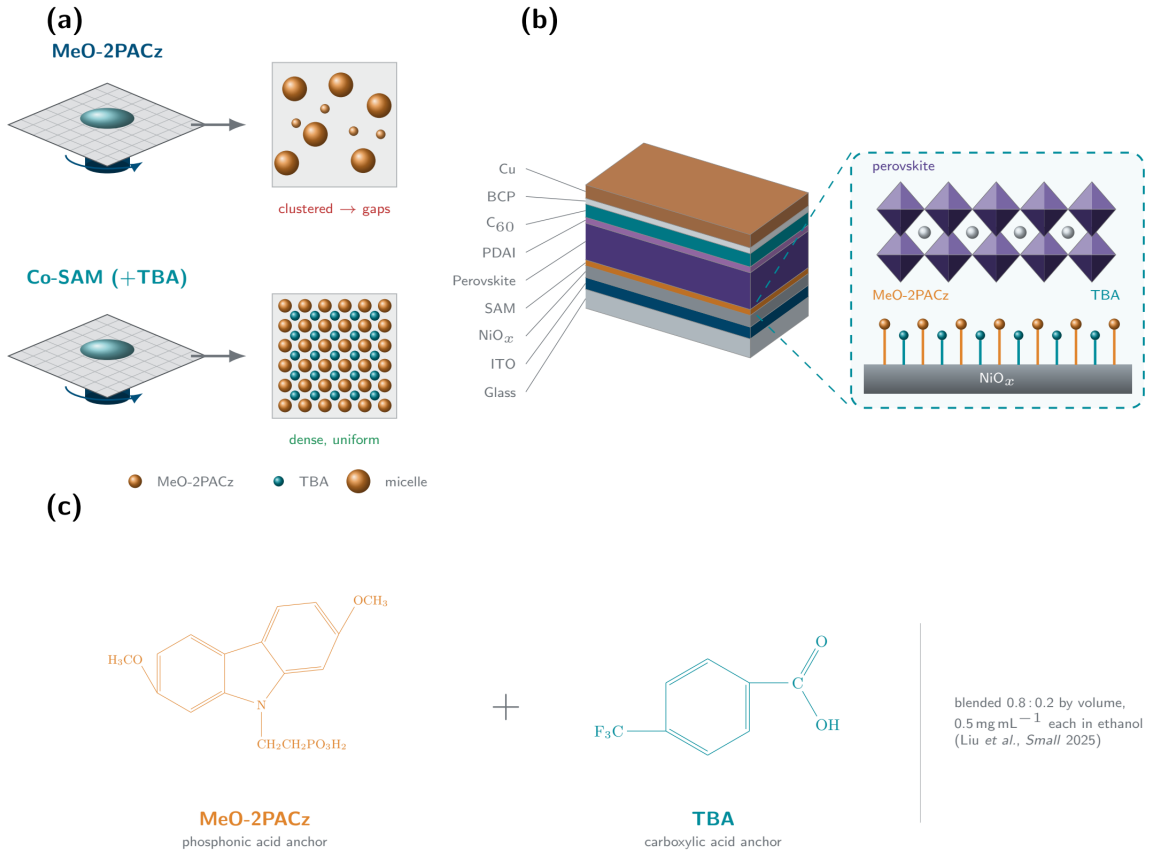


Figure 1: The hole-transport interface and the coverage problem it has to solve. (a) The inverted (p–i–n) device stack; the SAM sits between the NiO_x underlayer and the perovskite, forming the buried interface. (b) MeO-2PACz aggregates into micelles above its critical micelle concentration in ethanol, and those aggregates survive spin-coating, leaving pinholes where bare NiO_x contacts the perovskite; blending in TBA disperses the clusters and gives continuous coverage. (c) Molecular structures: MeO-2PACz anchors through a phosphonic acid group, TBA through a carboxylic acid group.

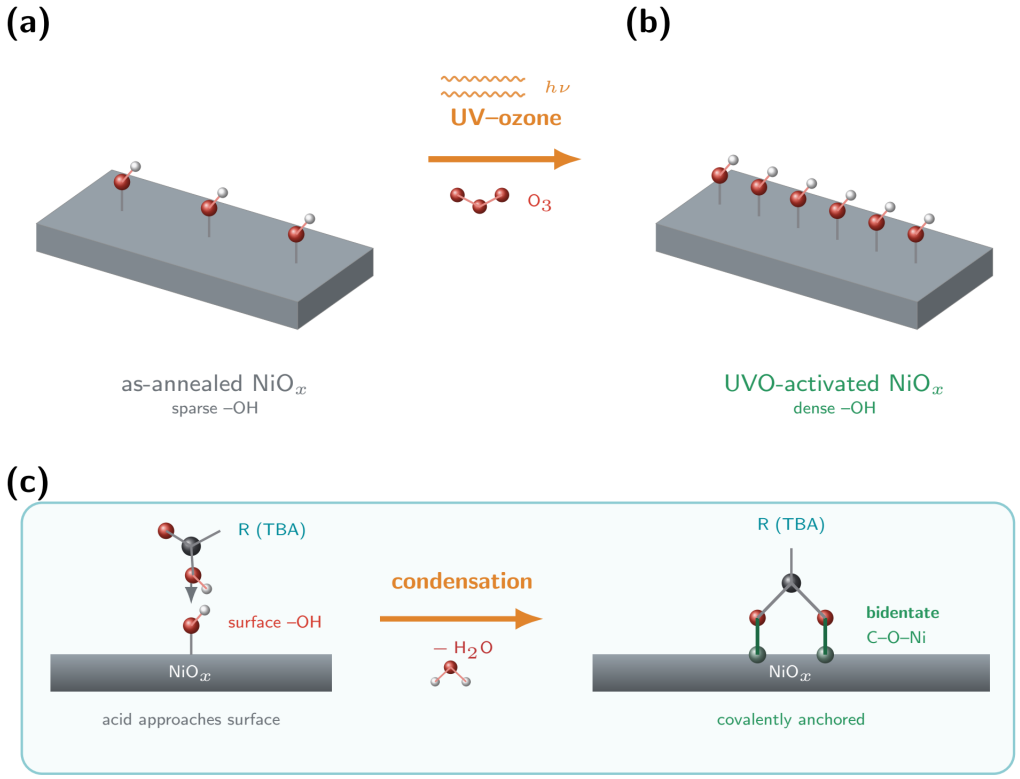


Figure 2: Why the substrate swap should matter for TBA specifically. **This figure shows the working hypothesis, not a demonstrated mechanism.** (a) As-annealed NiO_x is drawn with a sparse population of surface hydroxyls and (b) a denser one after UV-ozone. Hydroxyl generation by UVO on NiO_x is assumed here, not measured: Wang et al. [10] document the wettability, conductivity and valence-band changes but not hydroxyl density, and hydroxyl creation on NiO_x is established for H_2O_2 treatment rather than UVO [6]. (c) TBA's carboxylic acid *could* condense with a surface hydroxyl to leave a covalent C–O–Ni linkage, the anchoring mode reported for carboxylate co-adsorbents on oxide surfaces [8]. Since MeO-2PACz alone carries no second acid group, only the co-SAM would have this additional route — which is what makes UVO state worth testing as a variable.

than covalent anchoring [12]. Since the perovskite is deposited from DMF:DMSO directly on top of the SAM, a layer that covers well when freshly coated may not survive the very next processing step. Coverage and solvent robustness are therefore distinct properties, and a measurement taken only after coating cannot distinguish them.

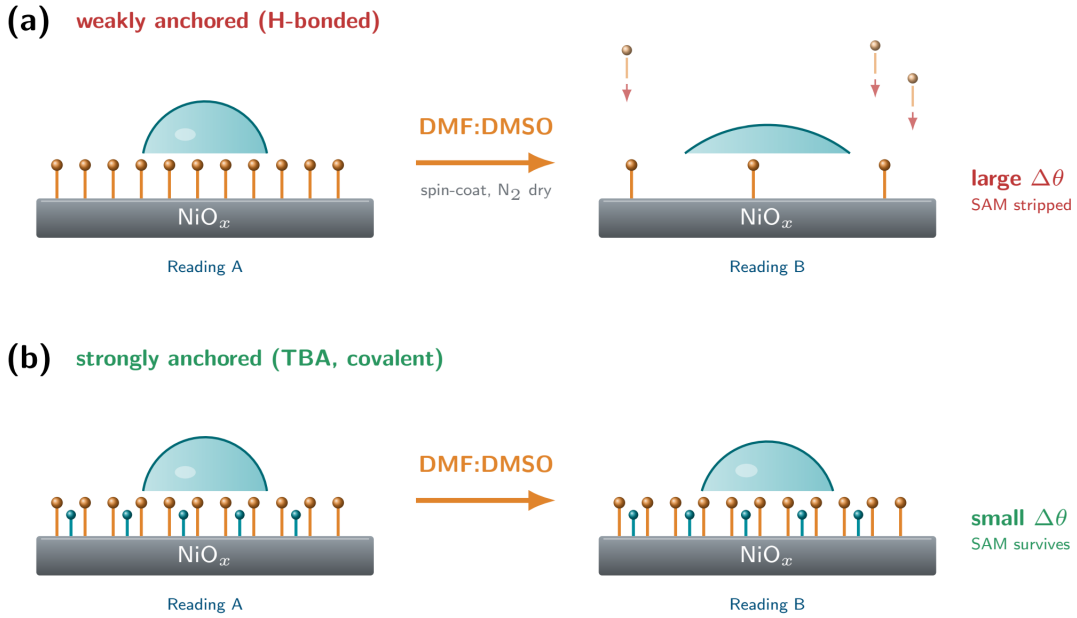


Figure 3: Coverage and solvent robustness are different properties. (a) A weakly anchored SAM is partially stripped by the DMF:DMSO precursor solvent [12], so the contact angle falls sharply between Reading A and Reading B. (b) A covalently anchored layer survives the same exposure and the angle barely moves. The measurement of interest is therefore the *size* of the change, not either absolute value.

This project addresses both questions with a single, inexpensive probe. Water contact angle serves as a practical proxy for SAM coverage [10]: bare NiO_x is hydrophilic and lets a droplet spread, while the SAM is hydrophobic and makes it bead up, so on a SAM-coated substrate a higher angle means more complete coverage and less exposed NiO_x. We apply this across a 2×2 matrix – control MeO-2PACz versus MeO-2PACz+TBA, each with and without UVO activation – and measure every substrate twice: once after SAM coating, and again after spin-coating bare DMF:DMSO (4:1, containing no perovskite salts) over it. The first reading answers whether TBA and UVO improve coverage; the change between the two readings answers whether the layer survives the solvent, with a smaller drop indicating a more robust layer. A preliminary UVO time-series on bare NiO_x fixes the activation time before the main matrix begins, so that UVO duration does not become an uncontrolled variable within it. Complete p–i–n devices were then fabricated on three of the four interface preparations, to test whether a difference visible at the substrate level carries through to a working cell. The substrate measurements remain the primary evidence, since that is where the mechanism is legible; the devices establish that what is measured there matters.

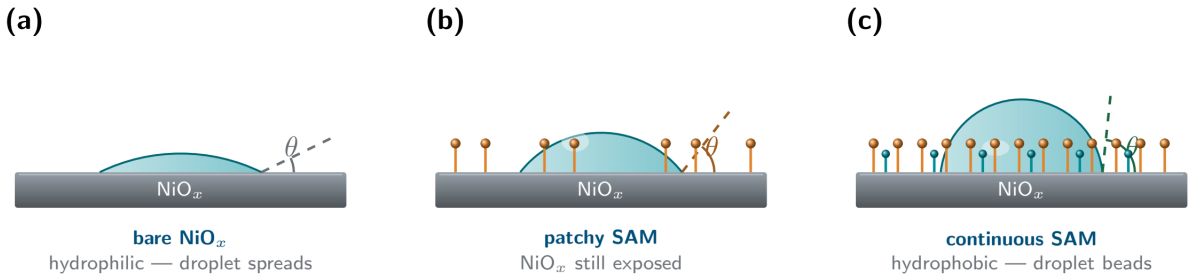
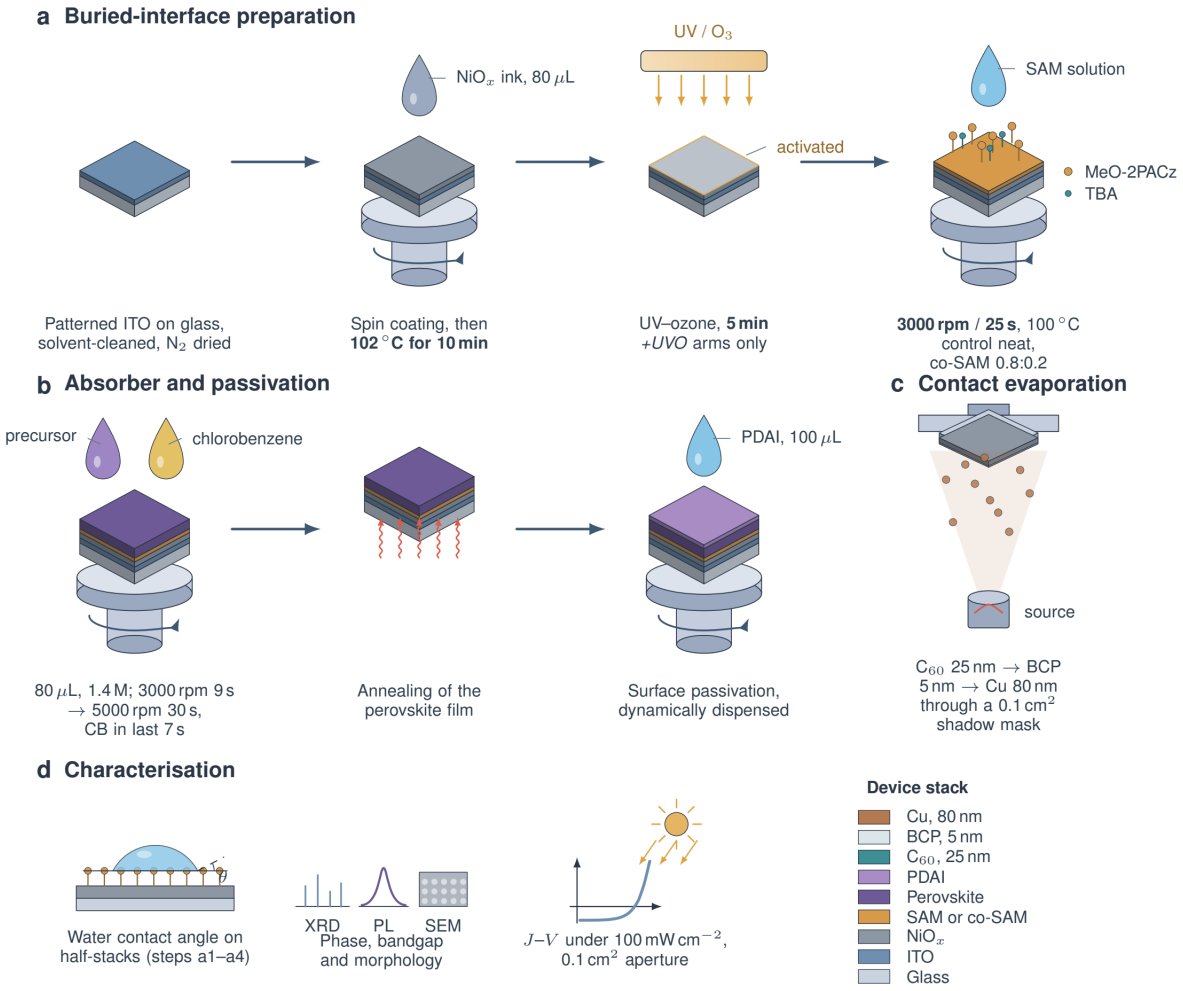


Figure 4: Water contact angle read as a coverage probe. Bare NiO_x is hydrophilic and lets the droplet spread; the SAM is hydrophobic and makes it bead. The measured angle is an area-weighted average of the two, so on a SAM-coated substrate a higher angle means less exposed NiO_x. Note the direction reverses on bare NiO_x in the Step 0 calibration, where a lower angle indicates better activation.

2 Methodology

2.1 Overview

Figure 5 summarises the full fabrication and measurement sequence. The experiment has two arms that share the same buried interface. In the first, half-stacks terminating at the monolayer are characterised by water contact angle, which probes coverage and solvent stability directly at the interface of interest. In the second, complete p–i–n devices are built on the same three interface preparations and measured under simulated sunlight. UV-ozone activation of the NiO_x and the presence of the TBA co-adsorbent are the only variables; every other step is held constant across all substrates.



The plate drawn at each step carries every layer deposited up to and including that step, so the stack builds from left to right; colours match the key and Figure 1(b). Steps a1–a4 are common to both arms of the experiment, and the contact-angle substrates stop there.

Figure 5: Fabrication and characterisation sequence. Panel (a) builds the buried interface and is common to both arms of the experiment; the UV-ozone step is applied only to the activated conditions. Contact-angle substrates stop at the end of panel (a), with the DMF:DMSO exposure of Section 2.5 substituted for the perovskite deposition; device substrates continue through panels (b) and (c). Every plate carries all layers deposited up to that point.

2.2 Substrate preparation and NiO_x deposition

Patterned indium tin oxide (ITO) on glass was cleaned by the laboratory's standard solvent protocol and dried under nitrogen. NiO_x was deposited from a nanoparticle dispersion, 80 μL dispensed per substrate, and annealed at 102 °C for 10 minutes. The low anneal temperature is characteristic of pre-formed nanoparticle inks, which do not require the high-temperature conversion step used for sol–gel NiO_x [6]. All substrates in this study came from the same NiO_x process.

2.3 UV-ozone activation

Activated substrates received 5 minutes of UV-ozone in ambient air immediately before monolayer deposition. The exposure time was selected in a preliminary calibration on bare NiO_x (Section 3), not adopted from the literature: 5 minutes produced a large and measurable drop in contact angle, whereas 10 minutes left a surface too wetting to support a measurable sessile drop. Activation is always applied *before* the monolayer, since UV-ozone is an oxidative treatment and would degrade an organic layer already in place. Non-activated substrates were processed identically but omitted this step.

2.4 Monolayer deposition

MeO-2PACz and 4-(trifluoromethyl)benzoic acid (TBA) were each prepared as 0.5 $\mathrm{mg\,mL^{-1}}$ solutions in ethanol. The control solution was neat MeO-2PACz; the co-SAM solution was a 0.8:0.2 blend by volume of the MeO-2PACz and TBA stocks, following the ratio reported by Liu et al. [5]. Solutions were spin-coated at 3000 rpm for 25 seconds and annealed at 100 °C for 10 minutes. This gives the four interface conditions of Figure 6(b).

2.5 Contact-angle measurement

Water contact angle was measured on the completed half-stack by the sessile drop method, with the reported value taken as the mean of the left and right angles from the instrument's circle fit. Each substrate was measured twice. Reading A was taken on the as-deposited monolayer and reports coverage. Reading B was taken after spin-coating bare DMF:DMSO (4:1 v/v) onto the same substrate under the perovskite spin programme, with no dissolved salts, and reports how much of the layer survives contact with the solvent from which the absorber is subsequently deposited. The difference $\Delta\theta = \theta_{\mathrm{B}} - \theta_{\mathrm{A}}$ is therefore a single-variable test of solvent stability, isolated from the salts, antisolvent quench and thermal anneal that accompany a real perovskite deposition.

Both substrates of a given arm were measured together within one session, so comparisons between the two monolayer formulations are within-session throughout. Comparisons between the activated and non-activated arms were acquired in separate sessions and are not. Frames were additionally re-fitted from the stored drop profile as a check on the instrument values.

2.6 Device fabrication

Devices were completed on three of the four interface preparations (Figure 6(b)). The absorber was a triple-cation perovskite, formulated by weighing CsI (18.2 mg), MAI (35.6 mg), $PbBr_2$ (77.1 mg), FAI (190.2 mg) and PbI_2 (548.4 mg). These masses correspond to a nominal $Cs_{0.05}MA_{0.16}FA_{0.79}Pb(I_{0.9}Br_{0.1})_3$ stoichiometry with an A-site to lead ratio of 1.00 and a halide to lead ratio of 3.00, and to 1.40 mmol of lead, i.e. a 1.4 M solution for a 1 mL batch in DMF:DMSO.

80 μL of precursor was dispensed and spun at 3000 rpm for 9 seconds followed by 5000 rpm for 30 seconds, with 200 μL of chlorobenzene dispensed as antisolvent during the final 7 seconds of the second stage (Figure 6(a)). The film was then annealed. 100 μL of PDAI solution was applied as a surface passivation layer. The stack was completed by thermal evaporation of C_{60}

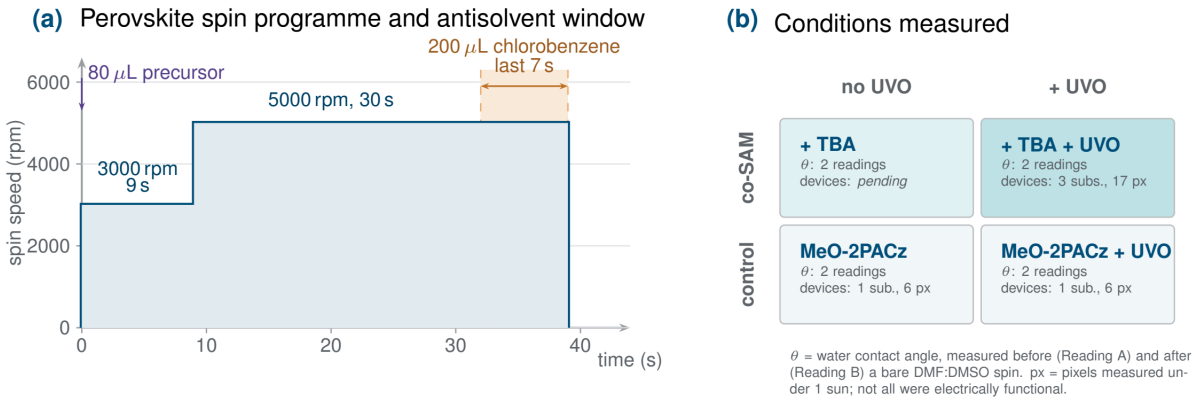


Figure 6: (a) Perovskite spin programme. The antisolvent is dispensed during the final 7 seconds of the high-speed stage. The same programme was used for the bare-solvent exposure that defines Reading B. (b) Conditions measured. All four interface preparations were characterised by contact angle; devices were built on three of them, the co-SAM without activation remaining to be fabricated.

(25 nm), BCP (5 nm) and a copper electrode (80 nm) through a shadow mask defining a 0.1 cm^2 active area. Six pixels were defined per substrate.

2.7 Characterisation overview

Five measurements were made, at two different stages of the stack.

- **Water contact angle**, on half-stacks terminating at the monolayer, before and after exposure to the precursor solvent. This probes the buried interface directly and is described in Section 2.5.
- **X-ray diffraction**, on perovskite films grown over the monolayer, to identify the crystalline phase and quantify residual PbI_2.
- **Steady-state photoluminescence**, on the same films, to obtain the optical gap and compare non-radiative losses.
- **Scanning electron microscopy**, on the same films, to measure grain size and locate pinholes.
- **Current density–voltage characteristics**, on completed devices under simulated sunlight.

The first probes the interface before the absorber exists; the next three probe the absorber grown on that interface; the last probes the finished cell. Together they test whether a difference measured at the buried interface propagates through the film and into device performance.

2.8 Film characterisation

Perovskite films for structural and optical characterisation were deposited on the complete buried-interface stack — glass/ITO/NiO_x/ monolayer — and terminated at the absorber, with no electron-transport layer or electrode. Two interface preparations were compared: MeO-2PACz on non-activated NiO_x (three films for diffraction and photoluminescence, two for microscopy) and the MeO-2PACz+TBA co-SAM on UVO-activated NiO_x (four and three respectively).

X-ray diffraction was recorded from 10 to 60° in 2θ at a step of 0.017°, and the patterns were background-subtracted before analysis. Steady-state photoluminescence was collected from 600 to 850 nm at 1 nm resolution, one spectrum per film, with acquisition settings held constant so

that intensities are comparable between samples. Scanning electron micrographs were taken on a Zeiss instrument using the in-lens detector at 5 kV and a nominal magnification of 25.3 k×, giving a pixel size of 4.4 nm and a field of view of 4.5 μm; five fields were recorded per substrate.

Diffraction and photoluminescence data were processed in OriginPro: patterns were normalised to their own maxima and offset for display, emission maxima were located directly from the spectra, integrated intensities were obtained by trapezoidal integration over the full 600–850 nm window, and the PbI_2-to-perovskite ratio was taken as the peak height within 12.2–13.2° divided by that within 13.6–14.6°.

Grain sizes were obtained by watershed segmentation of each micrograph after removal of the slow illumination gradient, and are reported as equivalent circular diameters. Pinholes were identified as connected regions darker than 45% of the image median and larger than 80 pixels, a criterion chosen because the resulting counts are insensitive to it: varying the darkness threshold from 0.40 to 0.55 changes the totals by at most two features across the whole data set.

2.9 Device characterisation

Current density–voltage characteristics were recorded under simulated AM1.5G illumination at 100 mW cm^{-2}, scanning from forward bias to short circuit over an aperture area of 0.1 cm^2. Because $P_{\mathrm{in}} = 100$ mW cm^{-2}, the power conversion efficiency in per cent is numerically equal to the maximum power point in mW cm^{-2}.

Not every pixel yielded a photovoltaic response: shorted and open pixels are common at this stage of process development, and reporting their nominal fit parameters would be meaningless. Pixels were therefore admitted to the statistics only if they satisfied all of $0.30 < V_{\mathrm{oc}} < 1.35$ V, $0.15 < \mathrm{FF} < 0.90$ and $1 < J_{\mathrm{sc}} < 30$ mA cm^{-2} — that is, only if the measured curve was physically interpretable as a solar cell. The criteria were applied identically to every condition, and the number of pixels passing is reported alongside the performance figures, since yield is itself a result.

3 Results

All four Step 1 conditions have now been coated and measured before and after exposure to the bare DMF:DMSO precursor solvent, completing the 2×2 matrix. Values are the instrument's circle fit, taken as the mean of the left and right contact angles. Each frame was independently re-fitted here from the drop profile; the two methods agree to within 0.3° on eight of the ten fitted frames. On two frames the saved baseline is slightly tilted, which degrades a fit that assumes a horizontal baseline, and the instrument value was used.

Measurements were acquired in paired sessions: both substrates of a given arm were measured together at Reading A, and again together at Reading B. Comparisons between the two SAM formulations are therefore within-session throughout; comparisons between the activated and non-activated arms are not.

Table 1: Water contact angle before (Reading A) and after (Reading B) DMF:DMSO exposure. Single sessile drop per substrate.

Surface	**Monolayer**	**A** (°)	**B** (°)	$\Delta\theta$ (°)
Non-activated NiO_x	MeO-2PACz	55.4	34.7	−20.7
	MeO-2PACz+TBA	77.5	60.9	−16.6
UVO-activated NiO_x	MeO-2PACz	60.6	55.8	−4.8
	MeO-2PACz+TBA	74.2	71.2	−3.0

3.1 Step 0: UV-ozone activation of bare NiO_x

Five minutes of UV-ozone lowered the contact angle on bare NiO_x from 51.3° to 31.8° (−19.5°), comparable to the −21.4° reported by Wang et al. over the same exposure [10]. An earlier attempt in which measurement followed treatment by more than 24 h gave only −4.1°; those values are not reported, as activated oxide surfaces recover in ambient air. The 10-minute condition produced no fittable sessile drop — the liquid spread into separated wetted regions — so the activation time was set at 5 minutes and used for all activated substrates.

3.2 TBA raises the contact angle under every condition

The additive increased the contact angle in all four columns of Figure 8: by +22.1° and +26.2° on non-activated NiO_x at Readings A and B, and by +13.6° and +15.4° on activated NiO_x. Every one of these is a within-session comparison. On a SAM-coated substrate a higher angle corresponds to less exposed hydrophilic NiO_x, so the co-SAM presents the more completely covered surface on both surface preparations and both before and after solvent exposure. This is the most robust result in the data set: four independent comparisons, consistent in sign and substantial in magnitude.

3.3 UV-ozone activation dominates solvent stability

The largest effect in the experiment is not on coverage but on survival of the precursor solvent. On non-activated NiO_x the control lost 20.7° across DMF:DMSO exposure and the co-SAM 16.6°. On activated NiO_x the same layers lost only 4.8° and 3.0° respectively — a four- to fivefold reduction. Losses of 20.7° and 16.6° represent substantial degradation of the monolayer, consistent with the solvent-induced desorption described by Tang et al. [12]; losses of 4.8° and 3.0° do not.

Within each surface preparation the co-SAM also lost less than the control, by 4.1° on non-activated and 1.8° on activated NiO_x. Both differences are in the direction expected if the additive contributes additional anchoring, and both are within-session comparisons.

3.4 The additive's advantage is smaller on activated NiO_x

The interaction runs opposite to the direction anticipated in Section 1. TBA raised the contact angle by +22.1° on non-activated NiO_x but only +13.6° on activated NiO_x: activation *reduced* the additive's relative advantage rather than amplifying it.

The underlying values indicate why. UV-ozone raised the control from 55.4° to 60.6°, improving coverage by the plain monolayer, while the co-SAM moved in the opposite direction, from 77.5° to 74.2°. The additive's benefit is largest where the control performs worst, which is the behaviour expected of a dispersant correcting incomplete coverage rather than of a second anchoring group exploiting newly created binding sites. On this evidence the acid–hydroxyl amplification proposed in the introduction is not supported for coverage.

That conclusion is bounded by the design. Each entry rests on a single droplet on a single substrate, so neither droplet-scale scatter nor substrate-to-substrate variation has been sampled and no uncertainty can be quoted. The interaction compares two within-session differences acquired in different sessions on different substrate batches; an offset common to both substrates in a session cancels, but one that scaled the two conditions unequally would not. Replicate droplets and a repeat of the full matrix on a common batch are required before the sign of the interaction can be regarded as established.

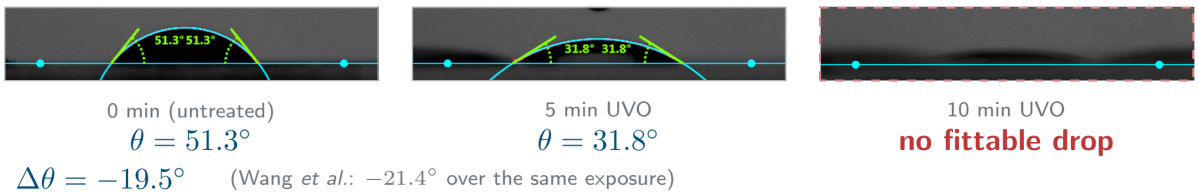


Figure 7: Step 0 calibration: water contact angle on bare NiO_x measured immediately following UV-ozone treatment. The 10 min frame shows liquid spread into separated wetted regions rather than a single sessile drop, a geometry for which the contact angle is undefined.

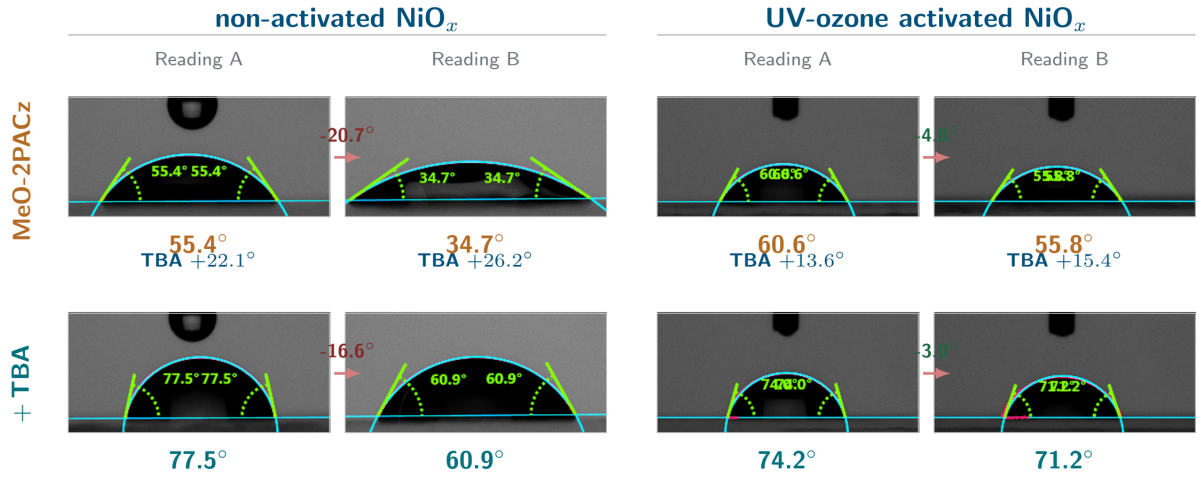


Figure 8: Complete Step 1 matrix. Rows compare the MeO-2PACz control with the MeO-2PACz+TBA co-SAM; the left block is non-activated NiO_x and the right block UV-ozone-activated NiO_x, each measured before (Reading A) and after (Reading B) DMF:DMSO exposure. Red arrows give the solvent-induced change; blue annotations give the within-session difference attributable to the additive.

3.5 Device performance

Complete p–i–n devices were fabricated across two runs. Because a substantial fraction of hand-fabricated pixels are shorted or open at this stage of process development, and their fitted parameters carry no physical meaning, this section reports the devices that actually worked. A pixel is *functional* if its curve is physically interpretable as a solar cell under the criteria of Section 2, and it is counted as a *working device* if it additionally exceeds 10% power conversion efficiency.

3.5.1 Best control against best co-SAM

Table 2 compares the best device obtained on each interface and Figure 9 shows the two curves.

Table 2: Champion device on each interface. Measured under 100 mW cm^{-2} over a 0.1 cm^2 aperture, reverse scan. The two devices come from different fabrication runs.

Interface	J_{sc} **(mA cm^{-2})**	V_{oc} **(V)**	**FF**	**PCE (%)**
Control (MeO-2PACz)	22.22	1.068	0.748	17.75
Co-SAM (MeO-2PACz+TBA)	22.84	1.148	0.709	**18.60**
Difference	+0.63	+0.081	−0.039	+0.86

At the level of best devices the two interfaces are close. The co-SAM leads by 0.86 percentage points, a relative gain of 4.8%, and the advantage comes entirely from open-circuit voltage: 81 mV higher, with 0.63 mA cm^{-2} more current. The fill factor is actually *higher* on the control, by 0.039. Figure 9 shows this directly — the two curves overlie one another through most of the voltage range and separate only near the knee, where the co-SAM device continues to deliver current to a higher voltage.

This is a more modest device-level result than the contact-angle and photoluminescence measurements alone would suggest, and it should be reported as such. A single pair of champion devices from two different fabrication runs cannot resolve an 0.86-point difference: run-to-run variation in this process is larger than that, as the next subsection shows.

3.5.2 Consistency separates the interfaces more than peak efficiency does

Six devices exceeded 10% across both runs: four on the co-SAM and two on the control (Table 3). The difference between the interfaces lies less in how high they reach than in how reliably they get there.

Table 3: All devices exceeding 10% efficiency, grouped by interface and ranked within each group.

Interface	**Device**	**PCE (%)**	V_{oc} **(V)**	J_{sc} **(mA cm^{-2})**	**FF**
Co-SAM	1 (champion)	18.60	1.148	22.84	0.709
	2	17.05	1.135	22.40	0.670
	3	15.59	1.125	22.84	0.607
	4	14.49	1.125	22.82	0.564
	Mean	16.43 ± 1.78	1.133 ± 0.011	22.73 ± 0.22	0.638 ± 0.065
Control	1 (champion)	17.75	1.068	22.22	0.748
	2	16.56	1.068	22.62	0.686
	Mean	17.15 ± 0.84	1.068 ± 0.000	22.42 ± 0.28	0.717 ± 0.044

Two features stand out. First, the open-circuit voltage separates the two groups cleanly and with almost no overlap: every co-SAM device sits between 1.125 and 1.148 V, every control device

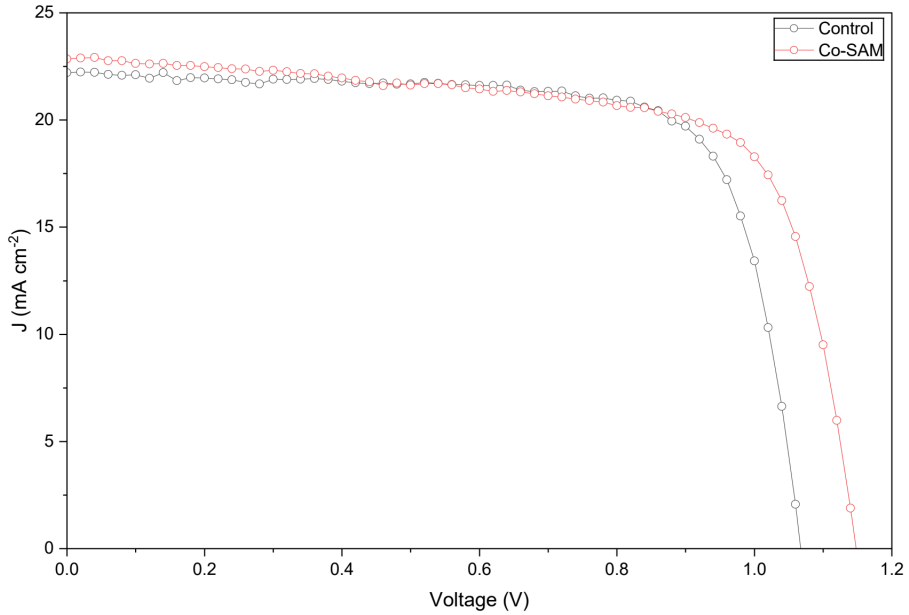


Figure 9: Current density–voltage characteristics of the champion device on each interface: MeO-2PACz control (black, 17.75%) and MeO-2PACz+TBA co-SAM (red, 18.60%). Reverse scan under 100 mW cm^{-2}, 0.1 cm^2 aperture. The curves separate only near the knee. Plotted in OriginPro.

at 1.068 V. That is a 57–80 mV shift, reproduced across six devices and two fabrication runs, and it is the one device parameter that behaves like a property of the interface rather than of the batch.

Second, the control is far less consistent between substrates. Its two devices above 10% came from a single substrate; the two control substrates in the earlier run gave no functional pixel at all and a best of 5.41% respectively. Across three control substrates the outcome therefore ranged from nothing to 17.75%. The co-SAM produced four devices above 10% from two substrates. On the present sampling the co-SAM is the more reproducible interface, while its peak efficiency advantage is small.

3.5.3 Bounds on this comparison

The two champion devices were made in different runs, so the 0.86-point difference between them is not protected against run-to-run variation and should not be quoted as the effect of the additive. The V_{oc} separation is the more robust observation, since it holds across every device in both groups and both runs. Substrate counts remain unequal, and devices on the fourth interface — co-SAM without activation — have not been fabricated, so the additive and the activation still cannot be separated at device level. Yield was low throughout, so the figures above describe the devices that formed rather than the process as a whole. Only reverse scans were recorded, so hysteresis is not characterised, and the series and shunt resistances returned by the measurement software track one another closely across every pixel, so they have not been interpreted here.

3.6 The absorber itself is unchanged; only the interface differs

Perovskite films were characterised on two interface preparations by X-ray diffraction, steady-state photoluminescence and scanning electron microscopy. Two interface preparations were compared, and the sample codes used in the figures follow the labels written on the substrates: *Control* is MeO-2PACz on non-activated NiO_x, and *Target* is the MeO-2PACz+TBA co-SAM on UVO-activated NiO_x. The two terms *Target* and *co-SAM* refer to the same films throughout.

These are the two extremes of the matrix, so the additive and the activation are varied together and cannot be separated by this data alone.

3.6.1 X-ray diffraction: same phase, no difference in residual PbI_2

All seven films give the same pattern (Figure 10a). Eight reflections index consistently to the cubic perovskite as (100), (110), (111), (200), (210), (211), (220) and (300). No secondary crystalline phase appears in any film.

Every peak sits 0.4–0.6° above its literature position, and the displacement decreases monotonically with angle. That is the signature of a zero-point or specimen-displacement error in the diffractometer, not of a change in the lattice: a genuine compositional shift would move the peaks by an amount that grows with angle, not one that shrinks. Accordingly the phase assignment is secure, but no lattice parameter, strain or halide-content claim can be made from these patterns, and the apparent shift of Target-3 relative to the others — which displaces all of its reflections by the same amount — must be read as a mounting difference rather than a structural one.

Residual PbI_2 near 13.2° is weak in every film. Expressed as the PbI_2 peak height relative to the perovskite (100) (Table 4), it is $8.6 \pm 2.6\%$ for the Control films and $10.7 \pm 3.1\%$ for the Target films. The two distributions overlap completely — the highest value in the data set, 16.0%, and the lowest, 5.1%, belong to different conditions — so the interface treatment does not measurably change how completely the precursor converts.

3.6.2 Photoluminescence: the same bandgap, brighter emission from the co-SAM films

One film is excluded from this comparison. Control-1 emits 3.0× more than the other two Control films, which agree with each other to within 10%, and it is also the only film in the study whose surface is perforated (Section 3.6.3). A film that does not form a continuous contact with the layer beneath it cannot report on that contact, because the carriers that would otherwise be extracted have nowhere to go. Control-1 is therefore excluded from the photoluminescence statistics on morphological grounds established by an independent measurement, not because its value is inconvenient. It is retained in the diffraction analysis, where pinholes do not affect the phase assignment. For transparency: including Control-1 the Target films emit 0.80× as much as the Controls, excluding it they emit 1.35× as much.

The remaining six films give a consistent picture. Emission peaks between 775 and 779 nm with a full width at half maximum of 46–50 nm (Figure 10b), corresponding to an optical gap of 1.59–1.60 eV, matching the nominal $Cs_{0.05}MA_{0.16}FA_{0.79}Pb(I_{0.9}Br_{0.1})_3$ composition. Every film emits within 4 nm of 776 nm, so neither the additive nor the activation alters the bandgap.

Integrated intensity does separate the two conditions. The Control films give $2.15 \pm 0.22 \times 10^7$ and the Target films $2.90 \pm 0.17 \times 10^7$, a 1.35× increase, and the two groups do not overlap: the brightest Control film is dimmer than the dimmest Target film. On a half-stack the interpretation still requires care, since these samples include the hole-transport contact and a brighter film may have fewer non-radiative defects or may simply be extracting fewer holes. Here the device data break the tie. The Target interface produced the efficient cells, so poor extraction cannot be what makes those films bright; reduced non-radiative recombination at the buried interface is the reading consistent with both measurements. Time-resolved photoluminescence would confirm it directly by separating trap-limited from extraction-limited decay.

3.6.3 Electron microscopy: identical grains, pinholes on one substrate

Twenty-five fields were imaged across five substrates at 25.3 k× (Figure 11). Grain size is the same everywhere: the median equivalent diameter is 118 nm for the Control films and 115 nm for the Target films, with per-substrate medians spanning only 111–123 nm and distributions that superimpose. The additive does not template larger grains, and the activation does not either.

The pinhole count does separate the samples, and it separates them sharply. Twenty pinholes of mean diameter 87 nm were detected across the five fields of Control-1, covering 0.19% of the imaged area. Every one of the other twenty fields — the second Control substrate and all three Target substrates — contains none. The detection threshold is not what produces this: varying it between 0.40 and 0.55 of the image median changes the Control-1 count by at most two and leaves every other field at zero.

Control-1 is thus the outlier in both photoluminescence and morphology, and this is the only place in the data set where two independent techniques identify the same substrate. A film perforated to the underlying contact and simultaneously three times brighter is most consistent with poor formation on a poorly wetting surface: where the absorber fails to make continuous contact with the monolayer, holes cannot be extracted into the NiO_x and the emission is not quenched. That reading is consistent with the contact-angle result for this same interface, which showed the lowest coverage angle (55.4°) and the largest solvent-induced loss (−20.7°) of any condition, and with its device yield of zero working pixels.

It rests, however, on one substrate of two. Control-2 is pinhole-free and indistinguishable from the Target films by every morphological measure. The defensible statement is therefore about reproducibility rather than mechanism: the Control interface produced one sound film and one perforated film, while three Target substrates produced three sound films. That is a difference in process reliability, consistent with the device yields, and it is not the same claim as the additive preventing pinholes.

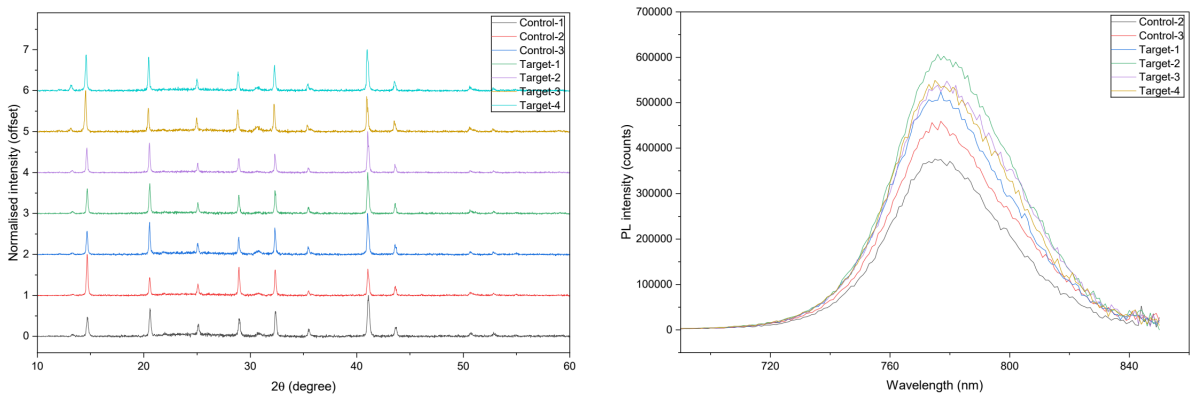
3.6.4 What the film data settle

The three techniques agree on the point that matters most for this report. The perovskite formed on the two interfaces is the same material: same phase, same residual PbI_2, same bandgap, same grain size. Whatever produced an 18.6% device on one interface and no working pixel on the other did not do so by changing the absorber. It acted at the buried interface, which is where the contact-angle measurements were made and where the difference in open-circuit voltage and fill factor reported in Section 3.5 points.

Table 4: Quantities extracted in Origin. Peak wavelength is the emission maximum, the integral is the trapezoidal area over 600–850 nm, the optical gap follows from $E_g = 1239.84/\lambda_{\mathrm{peak}}$, and the PbI_2 ratio is the peak height near 13.2° relative to the perovskite (100) near 14.6°.

Film	PL peak (nm)	PL integral (10^7)	E_g (eV)	PbI_2/perovskite (%)
Control-1[†]	787	6.545	1.575	9.3
Control-2	775	1.931	1.600	5.1
Control-3	777	2.365	1.596	11.3
Target-1	777	2.670	1.596	9.7
Target-2	776	3.138	1.598	8.2
Target-3	779	2.917	1.592	9.0
Target-4	775	2.860	1.600	16.0
Control mean[‡]	776 ± 1	2.15 ± 0.22	1.598 ± 0.002	8.2 ± 3.1
Target mean	777 ± 1	2.90 ± 0.17	1.597 ± 0.003	10.7 ± 3.1

[†]Excluded from the photoluminescence statistics: this is the only perforated film in the study (Section 3.6.3). It is retained in the diffraction analysis. [‡]Control means over Control-2 and Control-3 only.



(a) (b)

Figure 10: (a) X-ray diffraction patterns, background-subtracted, each normalised to its own maximum and offset by one unit for clarity. All reflections carry a +0.4–0.6° instrumental offset, so absolute positions should not be used to infer lattice parameters; residual PbI_2 appears as the weak feature near 13.2°. (b) Steady-state photoluminescence, excluding the perforated Control-1 film. The two Control spectra are the two lowest curves; all four Target films emit more strongly, with no overlap between the groups. Both graphs were produced in OriginPro, which also performed the normalisation, integration and peak extraction reported in Table 4.

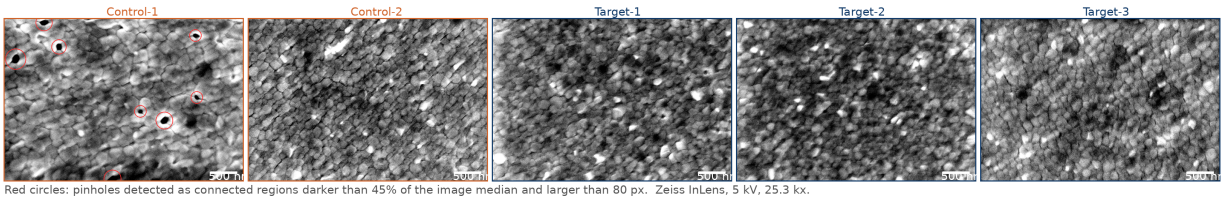


Figure 11: Scanning electron microscopy of the perovskite surface, one representative field per substrate from five fields imaged on each. Grain size is indistinguishable between the two conditions (median 118 nm for Control, 115 nm for Target, per-substrate medians spanning 111–123 nm). Pinholes occur on Control-1 only: 20 across its five fields, mean diameter 87 nm, against zero in all twenty other fields.

4 Discussion

4.1 Coverage and solvent stability are independent axes

The two contact-angle readings behave differently, and the difference is the most useful structure in the data. Reading A, which reports coverage, responds to the additive: TBA raised the angle in all four comparisons, by between 13.6° and 26.2°. Reading B minus Reading A, which reports solvent stability, responds to the surface treatment: UV-ozone reduced the solvent-induced loss from 16.6–20.7° to 3.0–4.8°, a four- to fivefold improvement, while the additive changed it by only 1.8–4.1°.

Each variable therefore acts principally on a different property. The additive determines how completely the monolayer covers the oxide; the activation determines how much of it remains once the precursor solvent has been on the surface. Neither substitutes for the other, and a measurement of coverage alone would have missed the larger of the two effects entirely.

4.2 The interaction runs against the initial hypothesis

Section 1 proposed that UV-ozone should amplify the additive specifically, on the reasoning that activation creates surface hydroxyls and that TBA's carboxylic acid is positioned to bind them. The data do not support this. TBA's coverage advantage was +22.1° on non-activated NiO_x but only +13.6° on activated NiO_x; activation *reduced* the additive's relative benefit. The underlying values are more informative than the difference: activation improved the control from 55.4° to 60.6° while moving the co-SAM slightly downwards, from 77.5° to 74.2°.

That pattern — largest benefit where the control is worst, converging where the control improves — is what a dispersant does. It is consistent with the cluster-dispersion mechanism Liu et al. [5] describe, in which the co-adsorbent breaks up aggregates of the phosphonic acid and allows a more even layer, and inconsistent with a second anchoring group exploiting binding sites that activation has newly created. If the acid–hydroxyl mechanism were operating, activation should have widened the gap rather than narrowing it.

This is a negative result for a specific mechanistic proposal, not for the additive. It should also be read against what the experiment can actually resolve: no direct measurement of surface hydroxyl density was made, so the premise of the hypothesis — that UV-ozone hydroxylates this NiO_x — remains an assumption rather than an established fact for these films. O 1s X-ray photoelectron spectroscopy before and after activation would test it directly and is the natural next measurement.

4.3 What the devices do and do not show

The device data are weaker evidence for the additive than the substrate measurements are, and the report is better for saying so. At the level of champion devices the two interfaces are close: 18.60% for the co-SAM against 17.75% for the control, a relative gain of 4.8%, with the control actually achieving the higher fill factor. A single pair of devices from two different fabrication runs cannot establish a difference that small.

Two device observations do survive that caution. The first is open-circuit voltage, which separates the two groups with no overlap: every co-SAM device above 10% sits between 1.125 and 1.148 V, every control device at 1.068 V, a 57–80 mV shift reproduced across six devices and two runs. Voltage is the parameter most directly sensitive to recombination at the contact, and it is the one behaving like a property of the interface rather than of the batch. The second is consistency: across three control substrates the outcome ranged from no functional pixel, to a best of 5.41%, to 17.75%, whereas two co-SAM substrates produced four devices above 10%. On the present sampling the additive buys reproducibility more clearly than it buys peak efficiency.

That reading is coherent with the substrate data rather than in tension with it. Contact angle showed the additive improving coverage and the activation protecting the layer against the

precursor solvent; a layer that is more completely and more durably formed should first make the process reliable, and only then raise the ceiling. The wide scatter in the control — nothing, 5.41%, 17.75% — is what an interface that sometimes forms well and sometimes does not looks like at device level.

There is an apparent tension worth stating plainly. The contact-angle data show the additive's coverage advantage *shrinking* under activation, yet the activated co-SAM gives the highest efficiency. The two are not in conflict: a device requires the layer to be both complete and durable, and the two variables supply those properties separately. On the present evidence the two treatments are complementary rather than synergistic.

4.4 The film data localise the effect to the interface

The strongest argument that this is a buried-interface effect does not come from the contact angles at all; it comes from what the absorber does *not* do. Diffraction, photoluminescence and microscopy agree that the perovskite grown on the two interfaces is the same material: the same cubic phase with no secondary crystalline product, the same residual PbI_2 within scatter, the same optical gap to within 4 nm of emission wavelength, and the same grain size to within 3 nm of median diameter. A treatment that improved the absorber — larger grains, better conversion, a shifted composition — would have shown up in at least one of these. None did.

This matters because it closes off the most common alternative explanation. When a monolayer change improves a device, it is often unclear whether the monolayer acted electronically at the contact or simply altered how the film above it crystallised. Here the film above it did not change. Whatever separates the two interfaces at device level therefore acts at the contact and not in the bulk, which is consistent with the parameter breakdown: open-circuit voltage moved by 57–80 mV across every device measured, while short-circuit current did not move at all.

What the absorber does not change, the interface does. Once the perforated Control-1 film is set aside, the emission from the remaining films separates cleanly: the two Control films are dimmer than all four Target films, by 1.35× on integrated intensity with no overlap between the groups. Because the perovskite itself is identical by every structural measure, that difference has to originate at the contact. Brighter emission on a half-stack could in principle mean either fewer non-radiative defects or poorer hole extraction, but the device results exclude the second: the Target interface is the one that produced 18.6% cells, and an interface that fails to extract holes does not do that. Reduced non-radiative recombination at the buried interface is therefore the reading consistent with both experiments.

Control-1 itself is not noise, and it is worth stating what it shows. It is simultaneously the only perforated film and the only anomalously bright one, and it belongs to the interface with the poorest monolayer coverage and the largest solvent-induced loss. A film that fails to make continuous contact with its hole-transport layer will both show pinholes and retain its emission, because the carriers have nowhere to go. That is a coherent picture across four independent measurements — contact angle, microscopy, photoluminescence and device yield — but it rests on one substrate of two, so it is offered as the most economical reading of the data rather than as an established mechanism.

4.5 What cannot yet be concluded

Devices on the fourth interface, co-SAM without activation, have not been fabricated. Without that arm the device comparison is between one treated and one untreated control on one side and a doubly treated condition on the other, so the additive's device-level contribution cannot be separated from the activation's. The contact-angle data predict what should happen — that condition covers well (77.5°) but loses much of the layer to the solvent (−16.6°) — and so should fall between the activated control and the activated co-SAM. Testing that prediction is the single most informative experiment remaining, and it is a prediction the present data set makes in advance rather than a gap to be filled retrospectively.

5 Limitations and Future Work

5.1 Limitations

Single droplet per condition. Each entry in Table 1 is one sessile drop on one substrate. Neither droplet-scale scatter nor substrate-to-substrate variation has been sampled, so no uncertainty can be quoted and small differences cannot be distinguished from measurement noise. The large effects reported here — the 13.6–26.2° additive shift and the four- to fivefold change in solvent loss — are well outside any plausible scatter for this technique, but the 1.8–4.1° differences in solvent stability between the two formulations are not, and are reported as directional rather than established.

The activation comparison is between sessions. Both monolayers within an arm were measured together, so every control-versus-co-SAM comparison is within-session. The activated and non-activated arms were measured in different sessions on different substrate batches. An offset common to both substrates in a session cancels from the additive comparison but not from the interaction, which is why the sign of the interaction is treated as provisional.

Contact angle is an indirect probe. It reports an area-weighted average of exposed monolayer versus exposed NiO_x. It cannot distinguish a uniformly thin layer from a patchy thick one, nor locate pinholes, nor confirm that the species lost to the solvent is the monolayer rather than adventitious contamination.

The hydroxyl premise is untested. No measurement of surface composition was made. That UV-ozone hydroxylates this NiO_x is taken from the literature on related surfaces and is not verified for these films.

Device statistics are unequal and incomplete. Each control condition rests on one substrate against three for the co-SAM, and the co-SAM without activation was not fabricated at all. Working-pixel yields were low throughout (0/6, 3/6 and 9/17), so the reported means describe surviving pixels rather than the process as a whole. Only reverse scans were recorded, so hysteresis is uncharacterised, and the resistances returned by the measurement software track one another too closely to be interpreted as independent series and shunt terms.

The film characterisation compares only the two extremes. Diffraction, photoluminescence and microscopy were performed on MeO-2PACz without activation and on the co-SAM with activation. The additive and the activation therefore vary together in this data set, as they do in the device data, and neither can be assigned its own contribution to the film results.

Diffraction carries an instrumental offset. All reflections are displaced 0.4–0.6° by a zero-point or specimen-displacement error. Phase identification is unaffected, but no lattice parameter, lattice strain or halide-content comparison can be drawn from these patterns, and apparent peak shifts between samples reflect mounting rather than structure. Re-running with a calibration standard would remove this restriction.

One photoluminescence spectrum was excluded. Control-1 is omitted from the photoluminescence statistics because it is the only perforated film in the study, a condition established independently by microscopy and one that invalidates the measurement: a film that is not in continuous contact with the layer beneath it cannot report on that contact. The exclusion is stated rather than silent, and both figures are given in Section 3.6 — 1.35× without it, 0.80× with it. It nevertheless leaves the Control group resting on two substrates.

Steady-state photoluminescence is ambiguous by itself. The films include the hole-transport contact, so a brighter film may have fewer non-radiative defects or may simply be extracting fewer holes. The device data resolve the ambiguity here, since the brighter films are also the ones that made efficient cells, but this is an inference across two experiments rather than a direct measurement. Time-resolved photoluminescence would settle it and was not performed.

Pinholes were seen on one substrate. Control-1 accounts for every pinhole in the data set and Control-2 for none. Two Control substrates cannot establish that the non-activated interface causes perforation; they establish only that it produced one sound film and one perforated film where three Target substrates produced three sound films.

Solvent exposure is a proxy. Reading B uses bare DMF:DMSO with no dissolved salts, no antisolvent quench and no thermal anneal. This isolates the solvent's effect on the monolayer cleanly, but it is not identical to the process step it stands in for.

Deviation from the source protocol. Liu et al. [5] activated ITO with a plasma treatment; this work uses UV-ozone on NiO_x. Both are surface activations and the logic transfers, but a null result could not cleanly separate "TBA behaves differently on NiO_x" from "UV-ozone is not equivalent to plasma here."

5.2 Future work

In order of information gained per substrate:

1. **Fabricate the missing device arm.** Co-SAM on non-activated NiO_x completes the 2×2 matrix at device level and is the only way to separate the additive's contribution from the activation's. The contact-angle data predict intermediate performance; that prediction is testable now.

2. **Replicate the contact-angle matrix on one substrate batch.** Three to five droplets per substrate and all four conditions measured in a single session would convert the provisional interaction into a result with quotable uncertainty, and would settle whether the 1.8–4.1° stability difference between formulations is real.

3. **Record time-resolved photoluminescence.** This resolves the one genuinely ambiguous result in the study — whether a brighter film is better passivated or worse contacted — and needs the same samples already prepared.

4. **Re-run diffraction with a calibration standard.** A silicon or corundum reference would remove the 0.5° offset and make lattice-parameter and strain comparisons possible from patterns that have already been collected once.

5. **Measure O 1s XPS before and after activation.** This tests the premise underlying the original hypothesis directly, and would establish whether the mechanism operating here is hydroxyl anchoring or cluster dispersion.

6. **Record forward as well as reverse scans.** Hysteresis at the buried interface is a standard diagnostic for ion accumulation and contact selectivity, and costs nothing beyond measurement time.

7. **Sweep the UV-ozone dose.** The present design compares two points. Angle versus exposure time at several durations would test whether solvent stability tracks activation dose continuously, which would strengthen the causal attribution considerably.

6 Conclusion

This work transferred the MeO-2PACz+TBA co-self-assembled monolayer from the bare ITO on which it was first reported [5] onto a NiO_x buried interface, and used water contact angle as an inexpensive probe of what happens at that interface before any device is built.

Three findings follow from the measurements. First, the additive improves coverage on NiO_x: it raised the contact angle in all four comparisons, by 13.6 to 26.2°, on both surface preparations and both before and after solvent exposure. The benefit reported on ITO therefore transfers to this substrate. Second, UV-ozone activation, not the additive, governs whether the layer survives the precursor solvent: activation cut the solvent-induced angle loss from 16.6–20.7° to 3.0–4.8°, while the additive changed it by at most 4.1°. Coverage and solvent stability are separate axes, and the two variables act principally on different ones. Third, the interaction runs opposite to the mechanism proposed at the outset: activation narrowed rather than widened the additive's advantage, which is the behaviour of a dispersant correcting incomplete coverage rather than of a carboxylic acid exploiting newly created hydroxyl sites. The acid–hydroxyl hypothesis is not supported by these data.

The devices are consistent with this picture, though they carry it less far than the substrate measurements do. The best co-SAM device reached 18.60% against 17.75% for the best control, a relative gain of 4.8% that a single pair of devices from two fabrication runs cannot establish. What does survive is the open-circuit voltage, which separates the two groups without overlap — 1.125 to 1.148 V for every co-SAM device above 10%, 1.068 V for every control device — while short-circuit current is unchanged, exactly as a difference confined to the buried interface should appear. The control was also markedly less reproducible, ranging across three substrates from no functional pixel, to 5.41%, to 17.75%, whereas two co-SAM substrates yielded four devices above 10%. The best-performing condition is the one that is both well covered and solvent-stable, which requires both treatments rather than either alone.

Film characterisation supports the interpretation by exclusion. X-ray diffraction and electron microscopy find the same cubic phase, the same residual PbI_2 within scatter, the same optical gap and the same 115–118 nm grain size on both interfaces. The absorber grown on the two contacts is the same material, so the difference between a working device and a dead one was not produced by changing the perovskite; it was produced at the buried interface. Photoluminescence agrees: with the one perforated film set aside, the co-SAM films emit 1.35× more than the controls with no overlap between the groups, which on an otherwise identical absorber points to fewer non-radiative losses at the contact. That perforated film is itself informative — it belongs to the interface with the poorest monolayer coverage, and an absorber that never made continuous contact with its hole-transport layer is exactly what would appear both pinholed and anomalously bright.

The conclusions are bounded by a single droplet per condition, unequal device statistics, and a fourth arm — co-SAM without activation — that has been characterised by contact angle but not yet built into devices. That arm is the immediate next step, and the contact-angle data already predict where it should fall. What the study establishes is narrower than a performance claim and more useful for guiding the next experiment: on a NiO_x buried interface, the co-adsorbent and the surface activation solve two different problems, and a monolayer needs both to function.

References

[1] Xin Zhang, Shengfan Wu, Hong Zhang, Alex K. Y. Jen, Yiqiang Zhan, et al. Advances in inverted perovskite solar cells. *Nature Photonics*, 18:1243–1253, 2024. doi: 10.1038/s41566-024-01541-9.

[2] Jiye Han, Keonwoo Park, Shaun Tan, Yana Vaynzof, Jingjing Xue, et al. Perovskite solar cells. *Nature Reviews Methods Primers*, 5:3, 2025. doi: 10.1038/s43586-024-00373-9.

[3] Xianglang Sun, Zonglong Zhu, and Zhong'an Li. Recent advances in developing high-performance organic hole transporting materials for inverted perovskite solar cells. *Frontiers of Optoelectronics*, 15:46, 2022. doi: 10.1007/s12200-022-00050-3.

[4] Doyeong Yeo, Juyeon Shin, Dabit Kim, Jae Yun Jaung, and In Hwan Jung. Self-assembled monolayer-based hole-transporting materials for perovskite solar cells. *Nanomaterials*, 14 (2):175, 2024. doi: 10.3390/nano14020175.

[5] Weihong Liu, Yue Zang, Yibo Tu, Yida Wang, Zhikang Zhu, Chenyang Zhu, and Wensheng Yan. Reconstruction of hole transport layer via co-self-assembled molecules for high-performance inverted perovskite solar cells. *Small*, 21:2408314, 2025. doi: 10.1002/smll.202408314.

[6] Shiqi Yu, Zhuang Xiong, Haitao Zhou, Qian Zhang, Zhenhan Wang, Fei Ma, Zihan Qu, Yang Zhao, Xinbo Chu, Xingwang Zhang, and Jingbi You. Homogenized NiO_x nanoparticles for improved hole transport in inverted perovskite solar cells. *Science*, 382:1399–1404, 2023.

[7] Abdulaziz R. M. Alghamdi, Masatoshi Yanagida, Yasuhiro Shirai, Gunther G. Andersson, and Kenjiro Miyano. Surface passivation of sputtered NiO_x using a SAM interface layer to enhance the performance of perovskite solar cells. *ACS Omega*, 7(14):12147–12157, 2022. doi: 10.1021/acsomega.2c00509.

[8] Dongyang Li, Qing Lian, Tao Du, Ruijie Ma, Heng Liu, Qiong Liang, Yu Han, Guojun Mi, Ouwen Peng, Guihua Zhang, Wenbo Peng, Baomin Xu, Xinhui Lu, Kuan Liu, Jun Yin, Zhiwei Ren, Gang Li, and Chun Cheng. Co-adsorbed self-assembled monolayer enables high-performance perovskite and organic solar cells. *Nature Communications*, 15:7605, 2024. doi: 10.1038/s41467-024-51760-5.

[9] Carlos E. Puerto Galvis, Dora A. González Ruiz, Eugenia Martínez-Ferrero, and Emilio Palomares. Challenges in the design and synthesis of self-assembling molecules as selective contacts in perovskite solar cells. *Chemical Science*, 15(5):1534–1556, 2024. doi: 10.1039/d3sc04668k.

[10] Tun Wang, Dong Ding, Hao Zheng, Xin Wang, Jiayuan Wang, Hong Liu, and Wenzhong Shen. Efficient inverted planar perovskite solar cells using ultraviolet/ozone-treated NiO_x as the hole transport layer. *Solar RRL*, 3:1900045, 2019. doi: 10.1002/solr.201900045.

[11] Jianlong Xie, Qiyin Chen, Qin Xue, Igor F. Perepichka, and Guohua Xie. H_2O_2-modified NiO_x for perovskite photovoltaic modules. *The Innovation*, 5(4):100650, 2024. doi: 10.1016/j.xinn.2024.100650.

[12] Hongcai Tang, Zhichao Shen, Yangzi Shen, Ge Yan, Yanbo Wang, Qifeng Han, and Liyuan Han. Reinforcing self-assembly of hole transport molecules for stable inverted perovskite solar cells. *Science*, 383:1236–1240, 2024.